Title

Characterization of the acoustic cavitation in ionic liquids in a horn-type ultrasound reactor.

Authors

Schieppati, Dalma
Mohan, Mood
Blais, Bruno
et al.

Publication Date

2024

DOI

10.1016/j.ultsonch.2023.106721

Peer reviewed

Ultrasonics Sonochemistry 102 (2024) 106721

Contents lists available at ScienceDirect

Ultrasonics Sonochemistry

journal homepage: www.elsevier.com/locate/ultson

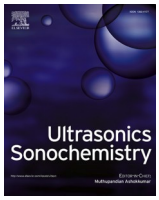

Characterization of the acoustic cavitation in ionic liquids in a horn-type ultrasound reactor

Dalma Schieppati [a], Mood Mohan [b,c], Bruno Blais [a], Kobra Fattahi [a], Gregory S. Patience [a], Blake A. Simmons [b,d], Seema Singh [b], Daria C. Boffito [a,*]

[a] Department of Chemical Engineering, École Polytechnique Montréal, C.P. 6079, Succ. CV, Montréal H3C 3A7, Québec, Canada
[b] Deconstruction Division, Joint BioEnergy Institute, 5885 Hollis Street, Emeryville, CA 94608, USA
[c] Bioscience Division and Center for Molecular Biophysics, Oak Ridge National Laboratory, Oak Ridge, TN 37831, USA
[d] Biological Systems and Engineering Division, Lawrence Berkeley National Laboratory, 1 Cyclotron Road, Berkeley, CA 94720, USA

ARTICLE INFO

Keywords:
Ultrasound
Acoustic pressure
Ionic liquid
Cavitation
Acoustic streaming
Active region

ABSTRACT

Most ultrasound-based processes root in empirical approaches. Because nearly all advances have been conducted in aqueous systems, there exists a paucity of information on sonoprocessing in other solvents, particularly ionic liquids (ILs). In this work, we modelled an ultrasonic horn-type sonoreactor and investigated the effects of ultrasound power, sonotrode immersion depth, and solvent's thermodynamic properties on acoustic cavitation in nine imidazolium-based and three pyrrolidinium-based ILs. The model accounts for bubbles, acoustic impedance mismatch at interfaces, and treats the ILs as incompressible, Newtonian, and saturated with argon. Following a statistical analysis of the simulation results, we determined that viscosity and ultrasound input power are the most significant variables affecting the intensity of the acoustic pressure field (P), the volume of cavitation zones (V), and the magnitude of the maximum acoustic streaming surface velocity (u). V and u increase with the increase of ultrasound input power and the decrease in viscosity, whereas the magnitude of negative P decreases as ultrasound power and viscosity increase. Probe immersion depth positively correlates with V, but its impact on P and u is insignificant. 1-alkyl-3-methylimidazolium-based ILs yielded the largest V and the fastest acoustic jets – 0.77 cm^3 and 24.4 m s^{-1} for 1-ethyl-3-methylimidazolium chloride at 60 W. 1-methyl-3-(3-sulfopropyl)-imidazolium-based ILs generated the smallest V and lowest u – 0.17 cm^3 and 1.7 m s^{-1} for 1-methyl-3-(3-sulfopropyl)-imidazolium p-toluene sulfonate at 20 W. Sonochemiluminescence experiments validated the model.

1. Introduction

Sonoprocessing finds numerous industrial applications, including chemical synthesis [1], surface modification [2], reaction acceleration [3], extraction [4], cleaning, and food processing [5]. Ultrasound (US) is a mechanical wave consisting of a cyclic succession of expansion and compression phases, during which liquid molecules are pulled apart and pushed together [5]. When the maximum change in pressure between compression and expansion phases, which is the pressure amplitude of the acoustic wave, exceeds the tensile strength of the liquid medium in the rarefaction regions, cavitation bubbles form. At high acoustic intensity, bubbles grow drastically and collapse during a compression phase when the radius of the bubble is tens to hundreds of times the equilibrium radius. This transient cavitation forms hot spots (5000 K and 500 bar) and liquid micro-jets, which elicit chemical and physical effects on the sonicated system [6,7]. Among the advantages of sonoprocessing we find the generation of reactive species and the enhancement of mass transfer, particularly in multiphasic systems [8]. One of the key factors that determine the outcomes of sonoprocessing is the nature of the solvent. Water has been the preferred solvent for most sonoprocessing applications, due to its abundance, low cost, and ability to generate reactive oxidizing species. However, some organic and inorganic compounds are insoluble or partially soluble in water. Moreover, some reactions either cannot take place or are extremely slow in presence of water. For example, the esterification of carboxylic acids with alcohols yields water as a by-product, which shifts the equilibrium towards the reactants thereby limiting the formation of the desired ester [9]. For these reasons, most organic and organometallic reactions require non-aqueous solvents, which are generally volatile, flammable, toxic, and their regeneration is energy intensive.

To obviate the undesirable properties of aqueous solvents for certain

* Corresponding author.
E-mail address: daria-camilla.boffito@polymtl.ca (D.C. Boffito).

https://doi.org/10.1016/j.ultsonch.2023.106721
Received 19 May 2023; Received in revised form 7 December 2023; Accepted 8 December 2023
Available online 13 December 2023

Nomenclatures

b	Damping factor
c	Speed of sound
C	Constant
CI	Confidence interval
C_P	Isobaric specific heat capacity
d	Probe immersion depth
D	Thermal diffusivity of gas
f	Ultrasonic frequency
F	Volumetric force
H	height
i	Imaginary unit
ID	Internal diameter
IL	Ionic liquid
k_m	Complex wave number
N	Bubble number density
P	Acoustic Pressure
P_A	Pressure amplitude
P_c	Pressure threshold required for cavitation
P_{max}	Maximum acoustic pressure (postive)
P_{min}	Minimum acoustic pressure (negative)
P_0	Static pressure (or undisturbed pressure in the bubble position)
P_{US}	Ultrasound input power
P_{vap}	Vapour pressure
R_{eq}	Equilibrium radius of bubble
R_0	Incipient radius of a monodispersed bubble
R_p	Probe radius
RMS	&Root mean square deviation
SCL	Sonochemiluminescence
t	Time
u	Maximum acoustic streaming surface velocity
US	Ultrasound
V	Active region volume
Z	Acoustic impedance

Greek letters

α	Acoustic attenuation from the intrinsic properties of the liquid
β	Bubbles volume fraction
γ	Specific heat ratio (adiabatic index)
μ	Dynamic viscosity
ρ	Density
σ	Surface tension
ϕ	Complex adimensional parameter
χ	Complex function
ω	Acoustic wave angular frequency
ω_0	Bubbles resonant frequency

applications, the scientific community shifted its attention towards ionic liquids (ILs). ILs are salts that are liquid at room temperature and that possess convenient intrinsic properties that make them attractive solvents for a plethora of chemical reactions. ILs are non-flammable, have high thermal stability, and do not emit volatile organic compounds. The combination of specific ions tunes the acidity [10], hydro- and lipophilicity [11], melting point [12], viscosity [13], surface tension and density [14], making ILs attractiv 'designer solvents' in the chemical field. Another advantage of ILs is their undetectable vapour pressure [15].

Because liquids and gases have different speeds of sound and compressibilities, there is an acoustic impedance (Z) mismatch at the bubbles' interface. Z is a measure of the resistance that a material exerts on the acoustic flow [16]. Acoustic cavitation relies on the violent collapse of bubbles. If bubbles do not implode, they scatter, reflect, or refract sound waves, leading to less intense sonochemical events. The number density and size of cavitation bubbles increases with the US input power. The attenuation of sound waves propagation is therefore an undesirable effect of cavitation at high acoustic intensity. As power increases, more bubbles collide and coalesce at the tip of the US probe, thereby forming a continuous layer of bubbles that adhere to its surface [17]. These bubbles are incapable of growing enough to implode because they undergo continuous cycles of coalescence and fragmentation, the latter imparted by the acoustic streaming jet forming below the sonotrode that pushes bubbles downwards. Furthermore, coalescence perturbs bubbles sphericity. Fattahi et al., [17] demonstrated that bubbles that remain spherical over several acoustic cycles and then collapse, lead to more intense sonochemical activity and larger active zones. Spherical bubbles are symmetric in shape, which means that the pressure inside the bubble is distributed evenly in all directions. They also have the minimum surface area for a given volume, so they require less energy to maintain their shape than other shapes, and they have a higher internal pressure for a given size, making them more prone to collapse. Additionally, spherical bubbles vibrate at the same frequency as the sound waves. This resonance amplifies the pressure fluctuations in the bubble, leading to rapid growth and collapse of the bubble. These factors make spherical bubbles more stable and easier to collapse than irregularly shaped bubbles.

The enthalpy of vaporization (ΔH_{vap}) of ILs is four to seven times higher than that of water and common organic solvents – e.g. ΔH_{vap} is 175.8 kJ mol^{-1} for 1-ethyl-3-methylimidazolium acetate, 40.6 kJ mol^{-1} for water, and 29.1 kJ mol^{-1} for acetone [18]. As a consequence of their low volatility, ILs generate a lower number of cavitation bubbles than water. This results in less numerous non-spherical bubble clusters, which translates into a lower attenuation of the acoustic energy and, in theory, larger active zones. Numerous variables affect the size of the active regions, including the solvent's thermodynamic properties. The application of US to intensify chemical reactions, given the significant diversity in properties amongst ILs, requires a deep understanding of the numerous factors influencing cavitation.

The state of the art surrounding the characterization of acoustic cavitation in ILs is rather limited compared to that of aqueous working media. We queried the Web Of Science Core Collection database with the keywords ((ionic liquid AND cavitation) OR (ionic liquid AND ultrasound)). The search yielded only 121 articles, published from 1993 to 2022. These articles were most published in: multidisciplinary chemistry (34), physical chemistry (21), chemical engineering (16), and acoustics (13). Ultrasonics Sonochemistry published 11 %, followed by the Journal of Chemical Physics (2.5 %) and Separation and Purification Technology (2.5 %). VOSviewer generated a bibliographic map based on the text in the titles, abstracts, and keywords of the 121 publications (binary counting, minimum number of term occurrence: 3). The dimension of a node is directly proportional to the occurrence of the term in the dataset, while the proximity of circles indicates how related the terms are. VosViewer identified 6 clusters (Fig. 1fig:map_us).

The green cluster groups publications concerning the application of US to ILs for synthetic purposes [20], while the yellow cluster those studying the cavitation bubble temperature [21,22] and sonoluminescence [15,23] under various conditions. The turquoise cluster gathers articles that make use of electrochemical or spectroscopic techniques for the investigation of cavitation activity [24]. The magenta and red clusters comprise US-assisted extractions and biomass pretreatments [25,26]. Finally, the blue cluster groups studies focusing on bubble dynamics in ionic aqueous solution [27]. In some instances, the

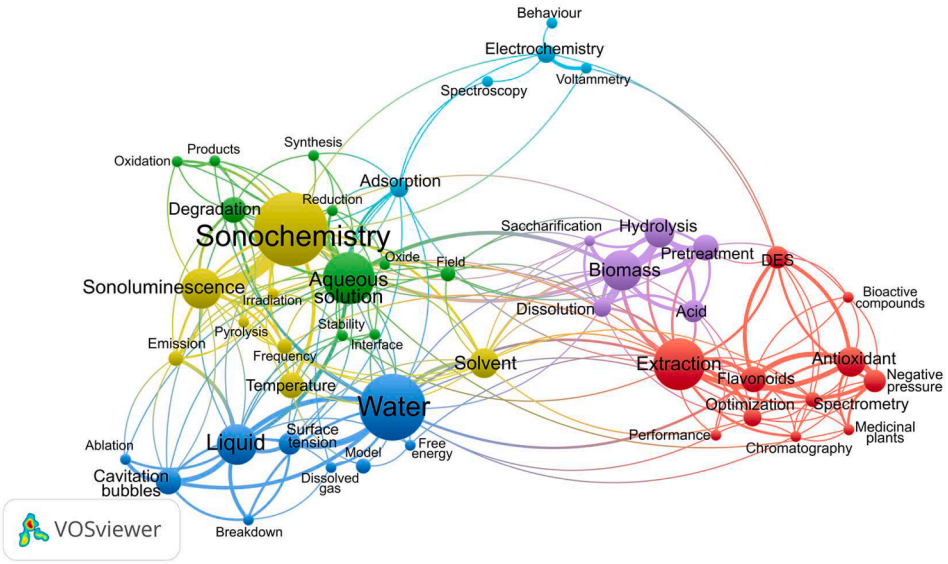

Fig. 1. VoSviewer bibliometric co-citation map of keywords. The database includes the top 49 keywords of the 121 articles that mention (ionic liquid AND cavitation) OR (ionic liquid AND ultrasound) from 1993 to 2023 [19]. The software assigns colours to terms that are related and positions them in proximity. The size of the circles is directly proportional to the number of occurrences of the term. With 11 terms, the red cluster is the largest one and it is centered on extraction (14 occurrences). The second largest cluster with 10 terms is the green one, centered on aqueous solutions (14 occurrences). The blue cluster counts 9 terms and centers on water (18 occurrences). The yellow cluster counts 8 keywords, and it centers on sonochemistry (20 occurrences). The magenta and turquoise clusters group (5) and (6) terms, respectively. The former centers on biomass (11 occurrences) while the latter centers on electrochemistry (5 occurrences). DES = deep eutectic solvents.

term *ionic liquid* represents ionic surfactants or inorganic salts rather than ionic liquids, hence why the numerous occurrences of *water* and *aqueous solution*.

Among these publications, only three address the characterization of the acoustic cavitation in ILs. Zhang et al., [28] studied the influence of the physical properties of 1-butyl-3-methylimidazolium hexafluorophosphate ([Bmim][PF_6]) on the cavitation dynamics at 20 kHz between 3 W and 17 W. By using the Flynn's equation [29] and considering an initial bubble radius of 4.5 μm, they determined that the cavitation intensity increases with the increase of amplitude and decreases with the increase of frequency. Moreover, they observed that, unlike for other solvents, the intensity of cavitation increases with the increase of the temperature of the bulk IL from 298 K to 323 K. This seems like a logical conclusion considering that the number of bubbles increases with increasing temperature. However, the temperature rise leads to a higher vapour pressure of the fluid and the gas content in the bubble increases, which consumes some of the collapsing energy thereby reducing the implosion intensity. [22] This uncharacteristic behaviour derives from the fact that (i) [Bmim][PF_6] has a null vapour pressure and its vapours do not enter the cavitation bubbles, and (ii) its viscosity decreases with the increase of temperature, resulting in the formation of more bubbles. Merouani et al., [30] studied the acoustic cavitation in room temperature methylimidazolium-based ILs saturated with air and compared it with that in aqueous medium. For their simulation, they adopted the Keller-Miksis equation and assumed the ILs as compressible fluids, isothermal expansion and adiabatic bubbles collapse, and negligible heat and mass transfer across the bubble–liquid interface. According to their model, the pressure and the temperature of the collapsing bubbles is much higher in 1-butyl-3-methylimidazolium bis (trifluorimethylsulfonyl)imide-based ionic liquids than in water. However, the experimental validation yielded a collapse temperature comparable to that of water. The authors ascribed this to the pyrolysis of ILs at the bubble–liquid interface, which lowers the bubble collapse temperature. Similarly, Kerboua et al., [31] applied the same equation to study the thermal effects induced by US on the dissolution of cellulose. They determined that in 1-butyl-3-methylimidazolium acetate (saturated with argon), at 200 kHz, a bubble of 5 μm requires an amplitude of at least 1.8 atm to reach transient cavitation, 60 times higher than that required by a bubble in water.

Despite the extensive literature available on acoustic cavitation, the limited number of studies that involve ILs present several shortcomings, including (i) the adoption of the Keller-Miksis equation, which models the dynamics of a single gas bubble in an infinite liquid domain exposed to a sound field and fails to consider its internal pressure, (ii) the omission of the acoustic impedance mismatch at interfaces (e.g. probe-liquid boundary), and (iii) the consideration of only one type of IL, thereby limiting the range of the properties studied. Moreover, the available studies neglect the thermodynamic characteristics of the liquid, the acoustic streaming jet velocity, and lack an experimental validation of the model.

In this work, we developed a model that quantifies the acoustic pressure, the volume of the active cavitation regions, and the surface velocity of the acoustic streaming jet in nine imidazolium-based and three pyrrolidinium-based ILs. The model takes into account the existence of multiple bubbles, considers the acoustic impedance mismatch at interfaces, and treats the ILs as incompressible, Newtonian, and saturated with argon. Because most commercial bench US processors operate at 20 kHz, we fixed the US operating frequency and investigated the influence of US power, probe immersion depth, and ILs' thermodynamic properties on the acoustic cavitation throughout the sonoreactor. We conducted a statistcal analysis to determine which independent variables affect the response factors the most, and validated the model through sonochemiluminescence experiments.

2. Mathematical model and governing equations

2.1. Acoustic pressure

The wave equation (Eq. (1) characterizes the variation of acoustic pressure, P, in space and time:

$$\frac{\nabla^2 P}{\rho} - \frac{1}{\rho c^2}\frac{\delta^2 P}{\delta t^2} = 0 \quad (1)$$

where ρ is the density of the liquid medium, c is the speed of sound in

m s^{-1}, t is time in s, and ∇^2 is the spatial Laplacian operator:

$$\nabla^2 = \frac{\delta^2 P}{\delta x^2} + \frac{\delta^2 P}{\delta y^2} + \frac{\delta^2 P}{\delta z^2} \tag{2}$$

To model the ultrasonic field, we considered the liquid medium was incompressible (Paragraph 2.4). Moreover, to apply Eq. (1) we assumed that shear stresses are absent or negligible, the sound waves propagating through the medium are linear, and pressure has a harmonic time dependence so that $P(r,t) = P(r)\cdot e^{i\omega t}$ [32], where ω is the acoustic wave angular frequency in rad s^{-1}. ω is the magnitude of the pseudovector quantity angular velocity, which in other words corresponds to the rate of the phase change of a sinusoidal wave and it is equal to $2\pi f$, where f is the ultrasonic frequency in Hz. Accordingly, Eq. (1) becomes the Helmholtz equation (Eq. (3), which describes the propagation of acoustic waves in liquid media [33].

$$\frac{\nabla^2 P}{\rho} + \frac{\omega^2}{\rho c^2} P = 0 \tag{3}$$

However, when ultrasound is applied to a liquid at a specific power and frequency, transient cavitation occurs. In this instance, bubbles form and accumulate the formation of bubbles and their consequent accumulation at the tip of the US probe is appreciable. In fact, bubbles scatter sound waves thereby attenuating their propagation [34,35]. A bubbly liquid is considered a continuous (fictitious homogeneous) medium if velocity and pressure variations change over distances larger than the inter bubble distance. The density of the medium then depends on the liquid, while compressibility on the gas content. If the frequency of ultrasound is below the lowest resonance frequency of bubbles, the distribution of gas in bubbles of specific size is negligible and only the total gas content per unit volume is significant [36].

Wijngaarden developed a series of equations that describe the one-dimensional turbulent flow that takes place in liquids containing bubbles [37,38]. Based on Wijngaarden's equations and the continuity equation, Commander and Prosperetti formulated a rigorous model for the propagation of pressure waves in liquids containing bubbles. Their model takes into account the damping effect of bubbles, which arises from viscous, thermal, and acoustic forces. The model assumes a negligible contribution of bubbles resonance and an incompressible fluid (constant density and null divergence of flow velocity). They validated their model by processing the experimental data sets of other existing works, with bubble radii ranging from 5 μm–3000 μm, frequencies in the range of 20 Hz to 10 MHz, and small gas volume fractions (10^{-5} to 10^{-2}). The model is accurate for gas volume fractions up to 2 % [39]. The Commander and Prosperetti's modified Helmholtz equation is:

$$\nabla^2 P + k_m^2 P = 0 \tag{4}$$

where k_m^2 is the complex wave number. For a monodisperse bubble distribution, k_m^2 is expressed as [40]:

$$k_m^2 = \frac{\omega^2}{c^2}\left(1 + \frac{4\pi c^2 N R_0}{\omega_0^2 - \omega^2 + 2ib\omega}\right) \tag{5}$$

where ω_0 is the bubbles resonant frequency b is the damping factor, R_0 is the incipient radius of a monodispersed bubble, N is the bubble number density, and i is imaginary unit. ω_0 is determined from:

$$\omega_0 = \sqrt{\frac{P_0}{\rho R_{eq}^2}\left(\mathrm{Re}\phi - \frac{2\sigma}{P_0 R_{eq}}\right)} \tag{6}$$

where P_0 is the undisturbed pressure in the bubble position (liquid static pressure), which corresponds to $P_{atm} + (2\sigma/R_{eq})$ where σ is the surface tension of the liquid. R_{eq} is the bubbles equilibrium radius considering direct contact coalescence and rectified diffusion, and ϕ is a complex adimensional parameter, a function of the specific heat ratio (or adiabatic index) of the gas inside bubbles (γ), and χ.

$$\phi = \frac{3\gamma}{1 - 3i\chi(\gamma - 1)\left[\sqrt{\frac{i}{\chi}}\cdot\coth\left(\sqrt{\frac{i}{\chi}}\right) - 1\right]} \tag{7}$$

χ is expressed as:

$$\chi = \frac{D}{\omega R_{eq}^2} \tag{8}$$

where D is the thermal diffusivity of the gas. The damping factor b in Eq. (5) corresponds to:

$$b = \frac{2\mu}{\rho R_{eq}^2} + \frac{P_0}{2\rho\omega R_{eq}^2}\mathrm{Im}\phi + \frac{\omega^2 R_{eq}}{2c} \tag{9}$$

where μ is the dynamic viscosity of the fluid. The bubble number density N depends on β, the volume of the gas fraction within the bubbles in the reactor with respect to the total volume:

$$N = \frac{3\beta}{4\pi R_0^3} \tag{10}$$

2.2. Active regions

The pressure threshold required for cavitation (P_c) depends on the nature and temperature of the sonicated liquid, and on its gas content (Eq. (11):

$$P_c = P_0 - P_{vap} + \frac{\frac{2}{3\sqrt{3}}\sqrt[3]{\left(\frac{2\sigma}{R_{eq}}\right)^2}}{\sqrt{P_0 - P_{vap} + \frac{2\sigma}{R_{eq}}}} \tag{11}$$

where P_{vap} is the vapour pressure of the sonicated liquid. To calculate and compare the cavitation zones that form inside the reactor, the acoustic pressure is set to P_c.

The identification and quantification of cavitation zones allows the comparison of various sonotrode geometries and positions with respect to the reactor. The cavitation zone generated by a conical tip is 1.56 times larger than that generated by a plane tip. However, a plane tip generates a faster acoustic streaming than conical tip [41], which results in better mass transfer. For this reason, and because they are the most commercially available, our simulation adopted a plane tip. Cavitation zones are quantified by using the acoustic pressure derived from Eq. (3) and Eq. (4) to display the attenuation elicited by cavitation bubbles.

2.3. Acoustic streaming

Sound waves elicit pressure fluctuations that induce fluid flow, which is referred to as acoustic streaming. US in the range 20 kHz to 20 MHz with power above 0.0004 W [42] in the form of a concentrated beam (horn-type probe) generates a turbulent acoustic stream within the sonicated system. The streaming velocity (u) is calculated from the Navier-Stokes equations (Eq. (12) [43,44,45,46].

$$\rho\left(\frac{\delta\vec{u}}{\delta t} + \vec{u}\cdot\nabla\vec{u}\right) = -\nabla\vec{P} + \mu\nabla^2\vec{u} + \vec{F} \tag{12}$$

Acoustic streaming originates from Bjerken forces acting on bubbles in an acoustic field. The intensity of these forces depends on the gradient of the acoustic pressure amplitude. Assuming that (i) the volume of the bubbles is constant, (ii) the amplitude below the sonotrode is above 1.8 atm (to achieve transient cavitation) [31,41], and (iii) the pressure wave emitted is a standing wave [16], the volumetric force (F) acting on the sonicated system is [41]:

$$F = -\beta\cdot\nabla|P| \tag{13}$$

We incorporated Eq. (13) into Eq. (12) to determine the flow pattern of the acoustic streaming generated upon the application of US. The

pressure gradient calculated through Eq.4 determines the direction of F.

When examining velocity, it is important to differentiate between point velocity and surface velocity. Point velocity is the velocity of a fluid at a specific point in the simulation domain. Surface velocity, on the other hand, is the velocity of the fluid along a surface in the simulation domain. While most articles in the literature report the point acoustic streaming velocity, we chose to analyze the surface acoustic streaming velocity for the following reasons:

(a) Acoustic streaming is heavily influenced by boundary effects, especially when the fluid is contained or near surfaces. Surface velocity directly captures the effects at these boundaries, whereas point velocities may ignore them, especially if the chosen point is away from such boundaries.
(b) Surface velocities provide an averaged value over the entire surface area, which can help in reducing noise or discrepancies that may be more apparent when considering a single point.
(c) When comparing results across different setups or experiments, analyzing surface velocities gives a more consistent parameter for comparison. Point velocities may vary significantly based on the precise location of the point, making comparisons less reliable.

2.4. Assumptions of the model

Eq. (3), Eq. (4), and Eq. (12) assume:

1. The liquid is incompressible and Newtonian. Because ILs consist of ions, they establish strong Coulombian ionic interactions, which makes them 90 % less compressible than organic solvents. The isothermal compressibility of imidazolium and pyridinium-based ILs is similar to water and molten salts across a wide range of temperature and pressure (298 K–343 K, up to 207 MPa) [47]: the longer the alkyl chain and the higher the temperature, the more compressible the IL. On the contrary, the higher the pressure, the less compressible the ILs become. The bulk modulus of a liquid, which is a measure of its resistance to a change in volume under pressure, is a quantitative indicator of the incompressibility of a liquid. The higher the bulk modulus, the less compressible the liquid. ILs have higher bulk modulus than water and other organic solvents. For example, at atmospheric pressure and room temperature the bulk moduli of 1-ethyl-3-methylimidazolium ethyl sulfate and water are 3.0 GPa [48] and 2.1 GPa [49], respectively.
2. The bubble to liquid volume ratio is low so that the cavitation bubbles do not affect the overall behaviour of the fluid.
3. The thermodynamic properties of the sonicated fluid are independent from temperature and bubble volume fraction.
4. The concentration of bubbles is homogeneous throughout the medium and β ranges between 10^{-4} and 10^{-1}. For $\beta > 10^{-1}$, bubbles scatter most of the incident acoustic waves. Hence, considering fractions larger than 10^{-1} does not contribute any meaningful physical significance to the model. The bubble density, hence β, linearly depends on the pressure amplitude, so that $\beta = C{\cdot}P$, where C is a constant [50,51]. Jamshidi et al., [40] investigated the ultrasonic wave propagation in a sonochemical reactor considering the effect elicited by the inhomogeneous bubble clusters and assumed that $\beta = 2 \times 10^{-9}{\cdot}P$. They validated the model in water and observed a high level of concurrence between the experimental outcomes and their model assuming this C value. For this investigation, we selected the same constant.
5. Ionic liquids are assumed to be saturated with argon gas. Despite the fact that ILs absorb more other gases like CO_2 [52], monoatomic gases have a higher adiabatic index ($\gamma = 1.67$ for He, Ne, and Ar, γ=2.5 for Xe vs.$\gamma = 1.30$ for CO_2), which results in higher temperature during the compression of a bubble that collapses adiabatically [36]. Although less soluble than Kr and Xe, produces more intense sonochemical events, regardless of bubble type [53]. solubility rates are high enough to create gaseous inclusions and induce acoustic cavitation upon the application of sufficient tensile strength [31]. The saturation of 1-ethyl-3-methylimidazolium acetate with argon originates monodispersed bubbles with a radius R_0 of 5 μm [31]. The equilibrium radius (R_{eq}) considering coalescence is about 50 times R_0 [54]. For this simulation we set R_{eq} equal to 250 μm.
6. The horn releases the acoustic radiation as Gaussian beams: the displacement amplitude across the face of the transducer plane varies so that it is the greatest in the middle and decreases as the radial distance from the center of the probe increases. In other words, the decrease in amplitude follows a Gaussian mathematical function.

3. Simulation

COMSOL Multiphysics 5.5 solved the equations in Paragraph 2 to determine the acoustic pressure distribution with and without bubble attenuation, and the acoustic streaming surface velocity profile. The equations were solved in a 2D axisymmetric configuration to reduce computation time.

The simulation consists of three steps (or studies), each dependent on the previous one:

1. The COMSOL Acoustic Module - Pressure Acoustic modelled a continuous wave excitation and solved Eq. (3) in the *Frequency Domain* considering the attenuation of the acoustic pressure arising from the intrinsic properties of the liquid medium (α). The study yields the effect of power and pressure amplitude on the acoustic field while neglecting the presence of cavitation bubbles in the medium and it provides an initial estimate for study 2.

$$\alpha = \frac{8\mu\pi^2 f^2}{3\rho c^3} \tag{14}$$

2. We included the attenuation due to bubbles by setting the Stabilized Convection-Diffusion Equation equal to Eq. (4) and by defining Eq. (5) to Eq. (10) within the parameters list. We calculated β by using the total acoustic pressure estimated in Study 1. Finally, we determined N and k_m^2 (Eq. (10) and Eq. (5) and solved Eq. (4) until steady state.

3. The COMSOL turbulent flow $k-\epsilon$ interface simulated the acoustic streaming turbulent jet. It solved the Navier-Stokes equations through a stationary study considering the acoustic pressure gradient derived from Study 2.

3.1. Geometry and boundary conditions

The sonochemical reactor selected for this study is a 100 mL borosilicate beaker (H = 8 cm, ID = 4 cm, thickness = 4.5 cm). The ultrasound probe is positioned vertically at the top of the beaker. The sonotrode is made of a titanium alloy, Ti-6Al-4 V, and has a diameter of 1.30 cm. The ultrasonic processor selected for the study operates at 20 kHz. The simulation domain corresponds to the volume of the sonicated liquid. We maintained the sonicated volume constant at 80 mL and the dimensions of the domain varies with the immersion of the probe. For example, with the probe immersed 2.00 cm, the dimensions of the domain are H = 6.58 cm and ID = 4.00 cm (Fig. 2fig:reactor).

3.1.1. Boundary conditions for acoustic pressure profile and active regions - studies 1 and 2

Jamshidi et al., [40] and Fang et al., [41] set the liquid-glass and liquid-probe boundaries as hard ($\frac{\partial P}{\partial x} = 0$ for $x = 0$) and the liquid–air boundary as soft ($P = 0$ vanishes). However, ultrasound reflects at interfaces with a Z mismatch. For a given material, Z corresponds to the product of its density and speed of sound. In this study, we applied the following boundary conditions (Fig. 2fig:reactor):

1. At the boundary liquid–air, Z= 1.2 kg/m^3 × 343 m/s.

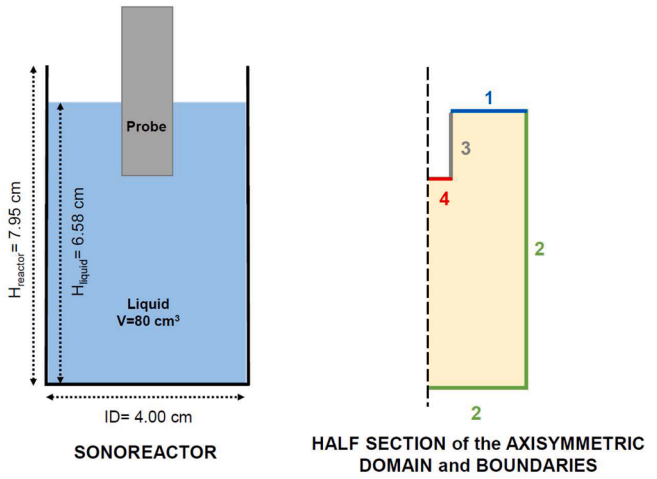

Fig. 2. Sonochemical reactor and half section of the axisymmetric computational domain with boundaries. The domain and the boundaries are an example assuming a liquid volume of 80 mL and for a 1.30 cm diameter probe immersed 2.00 cm.

2. At the boundary liquid-glass, $Z = 2230\ \mathrm{kg/m^3} \times 5640\ \mathrm{m/s}$ (for Pyrex).[1]
3. At the boundary liquid-probe, $Z = 4470\ \mathrm{kg/m^3} \times 4987\ \mathrm{m/s}$ (for a Ti-6Al-4 V probe).
4. At the tip of the probe, the pressure amplitude (P_A) was set to:

$$P_A = \sqrt{\frac{P_{US} 2c\rho}{\pi R_p^2}} \tag{15}$$

where P_{US} is the ultrasonic power delivered to the system calculated upon calorimetric calibration [55], and R_p^2 is the radius of the sonotrode.

3.1.2. Boundary conditions for acoustic streaming - study 3

For the simulation of acoustic streaming, we applied the the following boundary conditions (Fig. 2fig:reactor):

1. The liquid–air boundary was set as a pressure outlet with pressure set to 0.
2. No-slip boundary condition at the liquid-glass interface.
3. Slip boundary condition at the liquid-probe interface.
4. At the tip of the probe, Eq. (15) was set as the pressure inlet with inflow velocity directions (x and z) set to 1.3 and 0.03, respectively. The distance between the piezoelectric and the US emitting tip, which is 5 cm for the probe adopted for this investigation, dictated the inflow velocity direction. The turbulence length scale, which represents the size of the energy-containing eddies in the turbulent flow and depends on the turbulent kinetic energy and turbulent dissipation rate, was set to 0.07 R_p. Trujillo and Knoerzer, determined this correlation and we adopted it for our simulation as it was a suitable fit [56].

3.2. Mesh

Upon mesh sensitivity study, we opted for a 2D computational mesh consisting of triangles and quads (Table 1tab:mesh). We set the maximum dimension of each mesh element to be less than 1/8 of the ultrasound wavelength ($\lambda_{1/8,\ H2O} = 0.92$ cm and $\lambda_{1/8,\ IL} = 0.80$ cm to 1.15 cm [33]. We chose a fluid dynamics *normal mesh* for the domain (maximum size 0.09 cm, minimum size 0.004 cm, curvature factor 0.3, growth rate 1.15), and a fluid dynamics *finer mesh* (maximum size 0.056 cm, minimum size 8×10^{-4} cm, curvature factor 0.25, growth rate 1.10) along boundaries 2, 3 and 4 (Fig. 2fig:reactor).

The solution of Eq. (3) requires approximating the solution using a set of discrete points. For study 1 and study 2, we applied a quadratic Lagrange discretization as it provides a more detailed approximation of the solution, hence higher accuracy. For study 3, we applied a P2 + P1 fluid discretization (second order elements for velocity and first order elements for pressure) to solve the Reynolds-averaged Navier-Stokes equations as it captures the behaviour of fluid flow more accurately than other numerical methods [57].

Table 1
Meshing specifics for the three probe immersion depths.

Probe immersion	Triangles	Quads	Mesh area
cm			cm^2
0.5	5274	755	12.52
1	5189	760	12.29
2	5067	770	11.86

4. Ionic liquids and design of experiments

For this study, we selected twelve imidazolium- and pyrrolidinium-based ILs (Table 2tab:ILs) based on an acidity criterion that is of interest for a few ongoing investigations in our research group.

4.1. Prediction the thermodynamic properties of of ILs

Some of the thermodynamic properties of the ILs under investigation – specifically the isobaric specific heat capacity (C_P), speed of sound (c), density (ρ), surface tension (σ), and dynamic viscosity (μ) – have been determined experimentally and are available in the literature. Nevertheless, we predicted the thermodynamic properties for all the ILs with COnductor like Screening MOdel for Real Solvents (COSMO-RS) [18,58,59,60], group contribution method (GCM) [61,62], or via machine learning (ML) algorithms [63,64]. We compared the predicted values with the experimental ones and determined the root mean square deviation (RMSD) to identify flaws and further refined the prediction algorithms.

Table 2
The twelve ILs chosen for this study and their molar mass.

IL	Cation	Anion	Molar mass
			g mol^{-1}
[Etmim][Ac]	1-Ethyl-3-methylimidazolium	Acetate	170.2
[Etmim][Cl]	1-Ethyl-3-methylimidazolium	Chloride	146.6
[Etmim][$MeSO_4$]	1-Ethyl-3-methylimidazolium	Methyl sulfate	222.3
[Bmim][Ac]	1-Butyl-3-methylimidazolium	Acetate	198.3
[Bmim][Cl]	1-Butyl-3-methylimidazolium	Chloride	174.7
[Bmim][$MeSO_4$]	1-Butyl-3-methylimidazolium	Methyl sulfate	250.3
[Pyrr][Ac]	Pyrrolidinium	Acetate	131.2
[Pyrr][Cl]	Pyrrolidinium	Chloride	107.6
[Pyrr][H_2SO_4]	Pyrrolidinium	Hydrogen sulfate	169.2
[SPMim][Cl]	1-Methyl-3-(3-sulfopropyl)-imidazolium	Chloride	242.7
[SPMim][H_2SO_4]	1-Methyl-3-(3-sulfopropyl)-imidazolium	Hydrogen sulfate	304.3
[SPMim][PTS]	1-Methyl-3-(3-sulfopropyl)-imidazolium	*p*-Toluene sulfonate	378.5

[1] Considering the thinness of conventional beakers, it would be more fitting to adopt the acoustic impedance of air at the interface between the liquid and glass. However, this study primarily aimed to identify ionic liquids that maximize the active region volume for a separate ongoing project within our research group. In this project, we utilize an unconventional reactor with walls approximately five times thicker than traditional beakers. Consequently, we have chosen to define the acoustic impedance of the borosilicate glass at the reactor walls.

COSMO-RS predicted C_P (1 %≤ RMSD ≤ 23 %), μ (RMSD ≫ 10 %), and ρ (0.4 % ≤ RMSD ≤ 2.4 %). A ML algorithms determined σ (RMSD ≤ 2 %) and c (RMSD ≤ 1 %). The GCM developed by Sattari et al., [65] predicted C_P (3 %≤ RMSD ≤ 38 %). The GCMs by Lazzús et al., [66] and Gharagheizi et al., [61] predicted μ (RMSD ≤ 1 %). The elevated RMSD for C_P and μ only concerned protic ILs (e.g. [Pyrr][Ac]). High deviations stem from factors such as the proton transfer from acid to base, the pH of the acid/base, the proton affinity, and the presence of neutral molecules and ions in the mixture.

For the simulations, we adopted the experimental thermodynamic properties whenever available, and the predicted ones with the lowest deviations for those unavailable in literature (Table 3tab:ILsparam).

5. Design of experiments and statistical analysis

The dependant variables of this study are:

- the ultrasound power, P_{US}, three levels – 20 W (250 W/L), 40 W (500 W/L), 60 W(750 W/L)
- the probe immersion, d, three levels – 0.5 cm, 1 cm, 2 cm
- and the thermodynamic properties of the twelve ILs (Table 3tab: ILsparam)

The response variables are the minimum and maximum acoustic pressure generated (P_{min} and P_{max}), the volume of the acoustically active regions (V), and the magnitude of the maximum acoustic streaming surface velocity (u).

We opted for a full factorial design, for a total of 108 simulations. We conducted a statistical analysis to establish patterns and relationships within the data. To identify the key dependant variables that affect our response variables, we ran a preliminary predictor screening analysis with bootstrap forest partitioning (BFP). BFP algorithms randomly select subset of data and create multiple decision trees (100 trees in this instance) with aleatory features, and then take the average of all the tree's predictions. BFP reduces the chance of overfitting and improves the accuracy of the final prediction. According to the results of the predictor screenings, we then eliminated the non-significant dependant variables to find the model that predicted the response variables with an accuracy within a 95 % confidence interval (CI).

For the sake of clarity, in the Actual vs Predicted plots in the'Results and discussion' paragraph, the term *actual* refers to the simulated data points that were used to develop the prediction equation.

Table 3
Thermodynamic properties of water and ILs.

	C_P*	c	ρ	σ	μ	T_{ref}
	J kg K^{-1}	m s^{-1}	kg m^{-3}	mN m^{-1}	mPa s^{-1}	K
Water**	4184[E]	1498[E]	1000.0[E]	71.99[E]	1.00[E]	298.15
[Etmim][Ac]	1897[E]	1721[M]	1101.4[E]	38.17[E]	93.0[E]	298.15
[Etmim][Cl]	1955[C]	1854[M]	1123.9[E]	49.23[M]	65.0[E]	353.15
[Etmim][$MeSO_4$]	1568[C]	1770[M]	1284.2[E]	52.66[M]	78.8[E]	298.15
[Bmim][Ac]	1854[C]	1650[M]	1062.2[E]	35.31[E]	293.0[E]	298.15
[Bmim][Cl]	1963[C]	1802[M]	1055.7[E]	46.38[E]	123.0[E]	343.15
[Bmim][$MeSO_4$]	1613[C]	1676[M]	1212.2[E]	42.44[M,]	213.9[E]	298.15
[Pyrr][Ac]	1896[C]	1607[M]	1121.3[E]	33.50[M]	90.4[C]	298.15
[Pyrr][Cl]	1912[C]	1761[M]	1178.6[C]	56.08[M]	1379.6[G,]	298.15
[Pyrr][H_2SO_4]	1529[C]	1545[G,]	1424.1[E]	50.51[M]	321.8[C]	298.15
[SPMim][Cl]	1527[C]	1752[M]	1287.5[C]	38.42[M]	3921.0[G,]	298.15
[SPMim][H_2SO_4]	1392[C]	1647[M]	1395.3[C]	40.73[M]	1304.5[C]	298.15
[SPMim][PTS]	1451[C]	1519[M]	1269.5[C]	46.03[M]	7113.1[C]	298.15

*Isobaric, **Distilled, [E]Experimental [67], [C]COSMO-RS [18,58,59,60],[G]GCM,[M]ML[63,64].

6. Experimental validation of the model

To visualize the sonochemically active regions and acoustic streaming and validate the model, we conducted sonochemiluminesce (SCL) experiments in a dark room [17]. A 20 kHz and 500 W nominal power US processor from Sonics & Materials Inc. with a 13 mm replaceable tip Ti-6Al-4 V probe (115 μm displacement amplitude) sonicated 80 mL of liquid in a 4 cm ID x 7.5 cm H glass reactor.

We conducted experiments in water (at 298 K) and in [Bmim][Cl] (at 343 K). SCL in water required the addition of 0.15 g/L of 5-ammino-2,3-diidro-1,4-ftalazindione (Luminol, 97 %, Sigma Aldrich) and 4 g/L of sodium hydroxide (, 98 %, Sigma Aldrich). SCL in [Bmim][Cl] utilized 50 g of IL and 30 mL of a 0.20 g/L luminol and 4 g/L of solution. Luminol reacts with the hydroxyl radicals generated through water sonolysis and oxidizes to 3-aminophthalate in its excited state (3-APA*). 3-APA* then relaxes to 3-APA by emitting visible sonochemiluminescent blue light at a wavelength of 425 nm.

A Fujifilm X-T1 exposure-controlled digital camera and a lens with 56 mm focal length acquired SCL images with a shutter speed of 2 s and a F1.2 diaphragm aperture (sensibility ISO1600). We processed the images and measured the intensity of blue light emission signals with respect to the position in the sonoreactor. MATLAB (The Mathworks Inc., USA) subtracted the blank obtained in silent conditions (no background light) from the acquired SCL picture, and concealed parasite pixels with a blue filter. The software retained pixels with a light intensity above a 25/255 threshold. The lower threshold of 25 is the intensity of the blue light of the pixels in silent conditions, which corresponds to the background noise signal in the camera's blue channel. The upper threshold of 255 is the saturation of the 8-bits SCL images.

7. Results and discussion

7.1. Acoustic attenuation

Cavitation bubbles accumulate at the tip of the sonotrode and locally absorb and scatter sound waves, thereby reducing the cavitation intensity [34,35]. Neglecting the presence of bubbles results in higher acoustic pressure and larger active region volumes, as there is no attenuation of the acoustic wave travelling throughout the reactor (Fig. 3fig:bubbles). The absolute difference between V calculated neglecting acoustic attenuation and V computed by considering the presence of bubbles ranges between 161 % and 197 %. These results

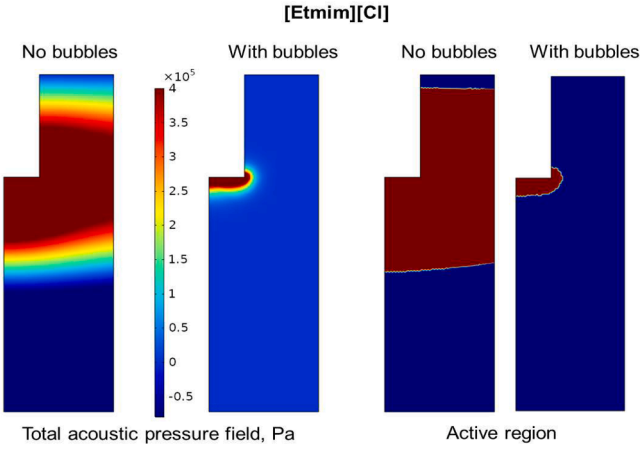

Fig. 3. Profiles of acoustic pressure field and active volume regions for [Etmim][Cl] at 60 W and$d$ = 2 cm. Comparison between simulations with (profiles on the right) and without (profiles on the left) acoustic attenuation elicited by cavitation bubbles. For [Etmim][Cl], the volumes of the active regions differ by 193 %.

demonstrate the significant impact that cavitation bubbles elicit on acoustic fields and active region sizes, highlighting the importance of accounting for their presence in models.

7.2. Acoustic pressure - P_{max} and P_{min}

Positive pressure and negative pressure during acoustic cavitation refer to the pressure increase and decrease, respectively, in the liquid as the sound wave propagates. Cavitation bubbles grow under positive pressure, while they collapse and release energy in the form of shock waves, heat, and light under negative pressure. P_{max} and P_{min} are the maximum and minimum acoustic pressure in the reactor, respectively.

The regression analysis of the simulation data (Fig. 4fig:APmaxreg) yielded the following equation for P_{max}:

$$P_{max} = 49.1 \cdot 10^4 + 11.5 \cdot 10^3 \cdot P_{US} \cdot \rho + 736.3 \cdot \sigma \quad (16)$$

P_{max} localizes under the sonotrode tip and it increases with the increase of P_{US}, ρ, and σ (Eq. (16). C_P, c, d, and μ do not have a significant effect on the magnitude of P_{max} within the reactor as they account for less than 0.5 % of the variance (Table 4tab:APmaxreg).

The behaviour of P_{min} is more complex and difficult to describe than that of P_{max}. Hence, we divided the dataset in two groups based on their μ. For ILs with $\mu \geq 1$ Pa s (high viscosity, HV), the regression (Fig. 5fig:APminHVreg) yielded the following equation:

$$P_{min,HV} = -38.8 \cdot 10^3 + 80.2 \cdot 10^3 \cdot \exp\left(\frac{-\mu \cdot \rho \cdot \sqrt{C_P}}{19.2 \cdot 10^4}\right) - 18.7 \cdot 10^3 \cdot \sqrt{\frac{P_{US} \cdot \sigma}{c}} \quad (17)$$

P_{min} decreases (becomes more negative) as μ, ρ, C_P, and c increase, and as P_{US} and σ decrease (Eq. (17). d explains less than 0.5 % of the variance and is insignificant (Table 5tab:APminHVreg).

For ILs with $\mu < 1$ Pa s (low viscosity, LV), the regression (Fig. 6fig:APminLVreg) provided the following equation:

$$P_{min,LV} = \frac{-4.15 \cdot 10^{-4} \cdot d}{-0.49 + d} \cdot \left(\frac{P_{US}}{\rho}\right)^{0.53} \quad (18)$$

$P_{min,LV}$ decreases as d and P_{US} decrease, and as ρ increases. μ, σ, c, and C_P account for less than 2 % of the variance each and their contribution to the prediction of $P_{min,LV}$ is statistically insignificant (p-value > 0.05) (Table 6tab:APminLVreg).

The magnitude of acoustic pressure is directly proportional to the speed of sound in a given medium. c determines how quickly the sound waves travel through the medium. As c increases, the particles in the medium vibrate more rapidly in response to the acoustic wave. More frequent vibrations increase the magnitude of acoustic pressure. Similarly, as the input P_{US} increases, so does the amount of energy transferred to the liquid: the magnitude of the generated sound waves - hence acoustic pressure - increases.

Despite having insignificant effects on P_{max}, μ substantially affects P_{min}. The higher the μ of a liquid, the larger the negative pressure required to break the cohesive forces keeping the liquid molecules together [68]. When the negative pressure exceeds the tensile strength of the liquid, the distance between molecules surpasses the critical molecular distance necessary to hold the liquid intact and cavitation bubbles form. High viscosity ILs, namely [SPMim]-based ILs, require lower P_{min} to cavitate. For example, [SPMim][PTS] ($\mu = 7113.1$ mPa s^{-1}) requires − 56 kPa−−58 kPa to cavitate at 60 W. On the contrary, [Etmim][$MeSO_4$] ($\mu = 78.8$ mPa s^{-1}) needs 8.21×10^{-8} Pa−−0.46 Pa to cavitate under the same conditions. Moreover, denser liquids have

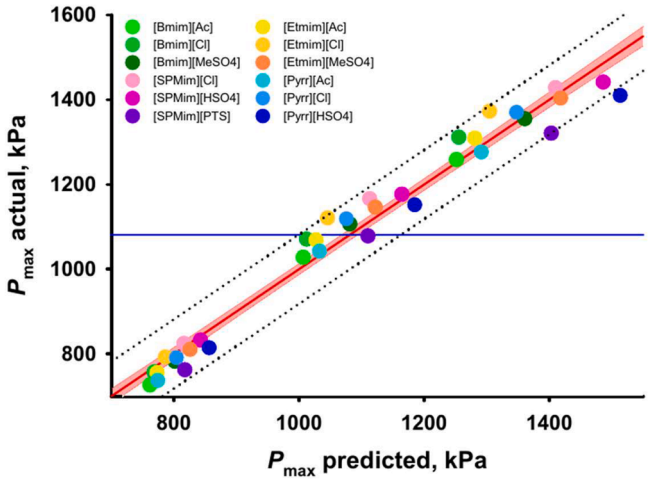

Fig. 4. Actual by Predicted plot of P_{max}, ▬ Regression, ▬95 % CI of prediction, RMSE = 40647.8, $R^2 = 0.972$, p-value < 0.0001, ▬ Mean of response (1080 kPa), • • • Prediction interval.

Table 4
P_{max} predictor screening. Statistic significance in descending order. *Portion of the variance explained by the predictor.

Predictor	Portion*
P_{US}	95.5 %
ρ	3.0 %
σ	0.7 %
C_P	0.3 %
c	0.2 %
d	0.2 %
μ	0.1 %

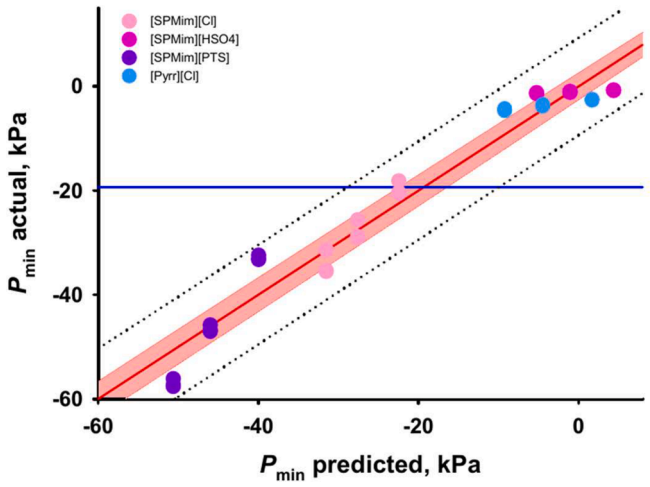

Fig. 5. Actual by Predicted plot of P_{min} for ILs with $\mu \geq 1$ Pa s. ▬ Regression, ▬95 % CI of prediction, RMSE = 4294, $R^2 = 0.955$, p-value < 0.0001, ▬ Mean of response (-19.34 kPa), • • • Prediction interval.

Table 5
Predictor screening analysis of P_{min} for ILs with $\mu \geq 1$ Pa s. Statistic significance in descending order. *Portion of the variance explained by the predictor.

Predictor	Portion*
μ	24.5 %
σ	24.2 %
ρ	19.0 %
C_P	18.5 %
P_{US}	7.7 %
c	5.8 %
d	0.3 %

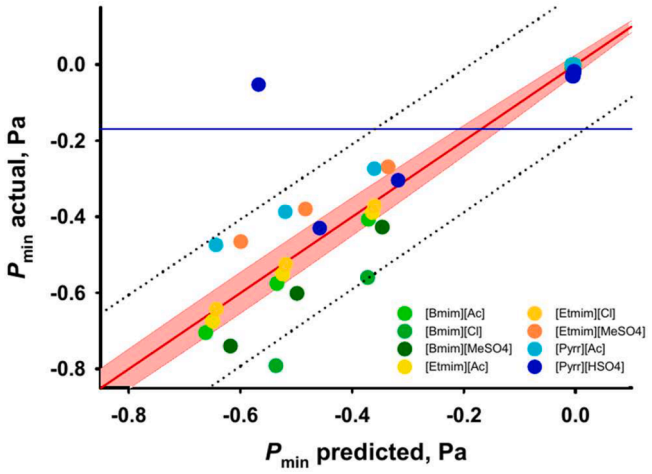

Fig. 6. Actual by Predicted plot of P_{min} for ILs with μ < 1 Pa s. ▬ Regression, ▬95 % CI of prediction, RMSE = 0.1057, R^2 = 0.877, p-value < 0.0001, ▬ Mean of response (-0.1813 Pa), • • • Prediction interval.

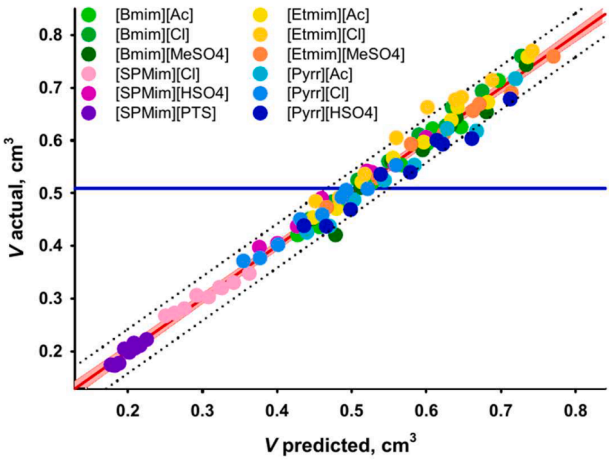

Fig. 7. Actual by Predicted plot of V. ▬ Regression, ▬95 % CI of prediction, RMSE = 0.0204, R^2 = 0.982, p-value < 0.0001, ▬ Mean of response (0.50 cm^2), • • • Prediction interval.

Table 6
Predictor screening analysis of P_{min} for ILs with μ < 1 Pa s. Statistic significance in descending order. *Portion of the variance explained by the predictor.

Predictor	Portion*
d	86.0 %
P_{US}	3.9 %
ρ	3.9 %
μ	1.9 %
σ	1.7 %
c	1.2 %
C_P	1.1 %

higher Z and require higher energy inputs to cavitate. This translates into cavitation bubbles requiring larger negative acoustic pressure to collapse in high density ILs.

The specific heat capacity indirectly affects the magnitude of acoustic pressure. When C_P increases, it becomes harder to compress the medium through which the sound waves are travelling: c increases and so does the amplitude of the sound waves, resulting in a higher magnitude of acoustic pressure.

The surface tension represents the strength of the cohesion forces that oppose the pressure variation during the compression and expansion phases of an acoustic cycle. When σ decreases, the attractive forces between the molecules at the surface decrease, which means that external forces easily displace the liquid. If σ is high, cavitation bubbles require more energy to expand and contract, and hence the amplitude of the sound wave will be lower. Conversely, if σ is low, the bubbles require less energy to expand and contract, resulting in a higher amplitude of the sound wave and therefore a higher P_{max}. Nevertheless, σ appeared to have insignificant effects (p-value > 0.05) on P_{min} at $\mu < 1$ Pa s. d does not have a significant effect on the magnitude of neither P_{max} nor $P_{min,HV}$, but it accounts for a large portion of the variance when $\mu < 1$ Pa s.

7.3. Active region volume V

The non-linear regression analysis of the simulated data (Fig. 7fig:ARVreg) yielded the following equation for the volumes of the active regions:Fig. 8.

$$V = 0.12 + 0.11 \cdot \exp\left(\frac{-\mu}{3845.19}\right) \cdot (P_{US})^{0.41} \cdot \left(\frac{C_P}{c}\right)^{-0.27} \cdot (d)^{0.13} \quad (19)$$

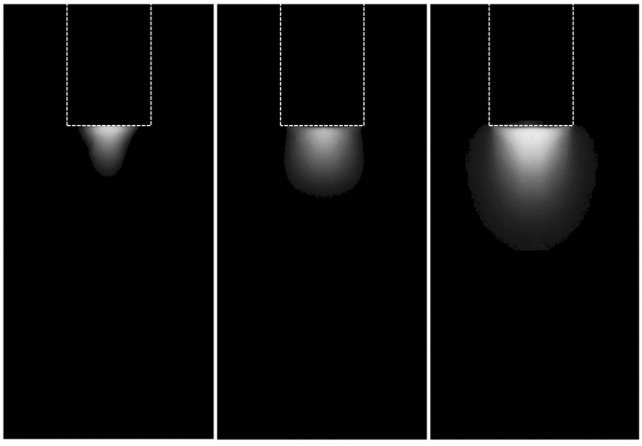

Fig. 8. SCL images in [Bmim][Cl] at 20 W (left), 40 W (center), and 60 W (right), with the probe immersed 2 cm. The dashed line represents the probe. V and u increase as P_{US} increases.

V increases as P_{US}, d, and C_P/c increase, and as μ decreases (Eq. (19). The intensity of US increases with the increase of input P_{US}. When the number of acoustic pressure cycles increases, cavitation bubbles become larger and more numerous, which then collapse more frequently and intensely, leading to larger V (Fig. 4fig:SCL_IL).

In water, the immersion depth of a 0.3 cm diameter probe does not affect the size of the cavitation region when exposed to P_{US} from 20 W to 60 W [69]. Instead, Fattahi et al., demonstrated that a 1.9 cm diameter probe at moderate power of 70 W (424 W/L power density) originates active zones below the probe and around its neck, resulting in larger V and higher cavitation yields [17]. Despite having the same probe, their sonicated volumes were 62 % and 106 % larger than in our study. In ILs, the active regions formed only under the sonotrode tip and V increased with d for all the ILs (Fig. 9afig:ARVvsPI and Fig. 9bfig:SCL_IL2). When the immersion depth increases, the hydrostatic pressure of the liquid surrounding the probe increases, causing P_c to increase as well. This, in turn, implies that the same intensity of ultrasound will subject a larger volume of liquid to cavitation. Moreover, the faster the sound waves travel through the medium (high c), the quicker and with greater magnitude the temperature and pressure change throughout the medium. This results in more rapid cavitation at lower pressures and in regions where cavitation might not otherwise occur, hence larger V.

On the contrary, changes in μ affect bubbles' size and distribution,

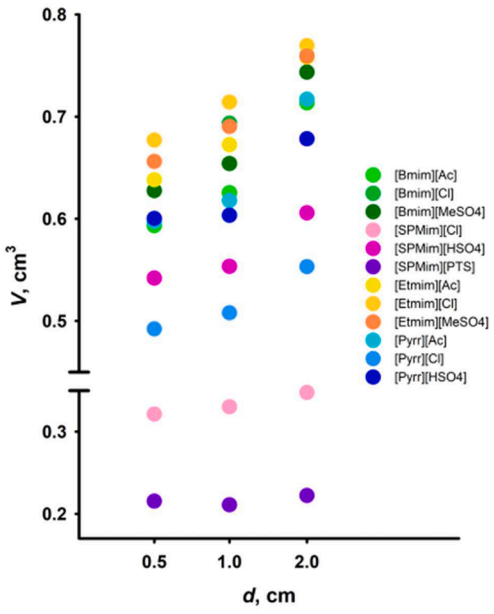

(a) V vs d at 60 W.

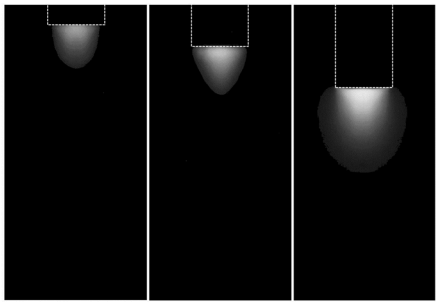

(b) Images of SCL in [Bmim][Cl] at 60 W with the probe immersed 0.5 cm (left), 1 cm (center), and 2 cm (right). V and u increase as d increases.

Fig. 9. There is a positive correlation between V and d, with a more pronounced enlargement when d increases from 1 cm to 2 cm.

hence wave attenuation [70]. The pressure fluctuations in viscous liquids are more gradual, leading to less shock waves and energy release during acoustic cavitation, resulting is smaller V (Fig. 10fig:ILvsH2O). The higher the c and the lower the μ of the ionic liquid, the larger the V. At 60 W and$d = 2$ cm, V was the largest for [Etmim][Cl] (0.77 cm^3) and the smallest for [SPMim][PTS] (0.22 cm^3) (Fig. 11fig:ARVbubbleplot).

For comparison, water is 65x and 7113x less viscous than [Etmim][Cl] and [SPMim][PTS], respectively. At 60 W and$d = 2$ cm, the V of water is 160 % and 800 % larger than that of [Etmim][Cl] and [SPMim][PTS], respectively.

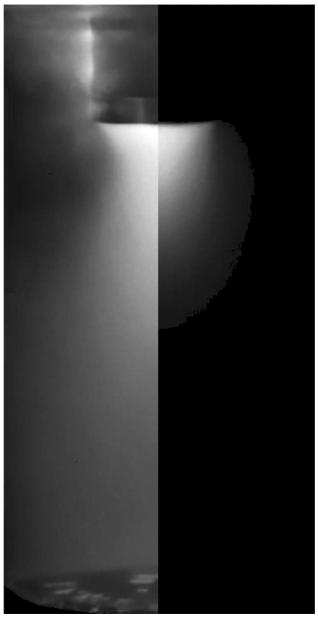

Fig. 10. Comparison between SCL images in water (left side) and [Bmim][Cl] (right side) at 60 W and $d = 2$ cm. V_{H2O} is 163 % larger than $V_{[Bmim][Cl]}$. The brighter areas at the bottom of the reactor in the SCL images in water are a result of light reflection caused by engraving on the bottom of the reactor. In water, active regions form around the neck of the probe.

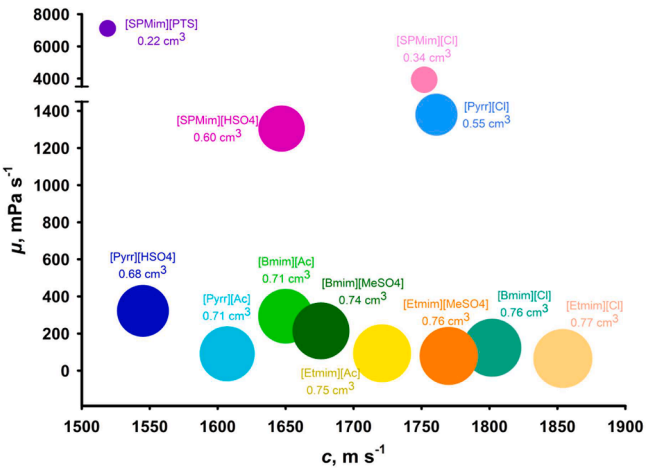

Fig. 11. Bubble plot representing the relationship between ILs' μ and c, with the bubble size representing V at 60 W and $d = 2$ cm. As c increases, the volume of cavitation active regions also increases, particularly for fluids with lower μ.

Similarly to what described in the previous section, the collapse of a bubble in a low-σ liquid produces a more violent collapse due to the lower cohesive forces holding the liquid molecules together at the surface. Contrary to what expected, ρ positively correlates with V. When ρ increases, the pressure required to cause cavitation also increases. This is because cavitation occurs when the local pressure in the liquid falls below the vapour pressure of the liquid, which is related to its density. Therefore, a denser liquid requires a higher pressure to achieve the same level of cavitation. σ and ρ did not have a significant effect on the volume of the active regions within the reactor and each accounted for less than 1.5 % of the variance (Table 7tab:ARVreg).

7.4. Maximum acoustic streaming surface velocity u

The regression analysis (Fig. 12fig:ASVreg) yielded the following equation for the maximum acoustic streaming surface velocities:

Table 7
Predictor screening analysis of V. Statistic significance in descending order. *Portion of the variance explained by the predictor.

Predictor	Portion*
μ	58.7 %
P_{US}	23.6 %
C_P	8.2 %
c	3.8 %
d	3.3 %
σ	1.3 %
ρ	1.1 %

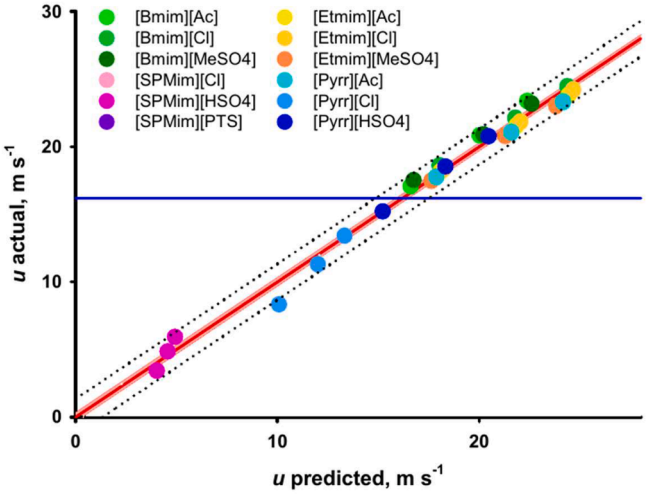

Fig. 12. Actual by Predicted plot of u. ▬ Regression, ▬95 % CI of prediction, RMSE = 0.6478, $R^2 = 0.992$, p-value < 0.0001, ▬ Mean of response (16.25 m s^{-1}), • • • Prediction interval.

$$u = 1.7 + 6.3 \cdot \exp\left(-\frac{\mu \cdot \rho^{-0.06}}{0.2 \cdot 10^4}\right) \cdot \left(\frac{P_{US}}{c}\right)^{0.3} \cdot \left(\frac{c}{\rho}\right)^{0.4} \cdot \left(\frac{C_P}{\rho}\right)^{-0.07} \quad (20)$$

u increases as P_{US}, c, and C_P increase, and as μ and ρ decrease (Eq. (20). As P_{US} increases, so does the gradient of the acoustic pressure amplitude (primary acoustic radiation force), which results in more intense Bjerknes forces, hence higher u. Acoustic waves also interact with the acoustic streaming flow (secondary acoustic radiation force), which contributes to the increase in u with increasing P_{US} (Fig. 13).

When c increases, the wavelength of the acoustic wave also increases, which leads to a larger acoustic radiation force and a stronger acoustic streaming flow. As mentioned before, C_P affects the amplitude of sound waves. When C_P increases, the medium through which sound waves travel becomes less compressible, which results in an increase of the amplitude of waves and higher c. [Etmim][Cl] and [Bmim][Cl] have the highest c and generated the fastest acoustic jets with maximum surface velocities of about 24 m s^{-1} (Fig. 14fig:ASVvsc). Similarly, because the acoustic pressure amplitude and gradient are both proportional to the density of the fluid, the primary acoustic radiation force is also proportional to the density of the fluid. Therefore, a higher ρ of the liquid medium leads to a stronger acoustic radiation force and a higher u.

On the contrary, u decreases as μ increases (Fig. 15fig:ASV_20W). Like for V, the more gradual pressure fluctuations in viscous liquids lead to less intense shock waves formation and energy release during bubbles collapse, resulting is smaller jets with lower u. In fact, [SPMim]-based ILs, which all have viscosity above 1300 mPa s^{-1}, yielded the lowest maximum streaming velocity, ranging from 1.7 m s^{-1} to 14.2 m s^{-1}.

σ and d did not have a significant effect on the magnitude of u within the reactor and they account for less than 0.2 % of the total variance

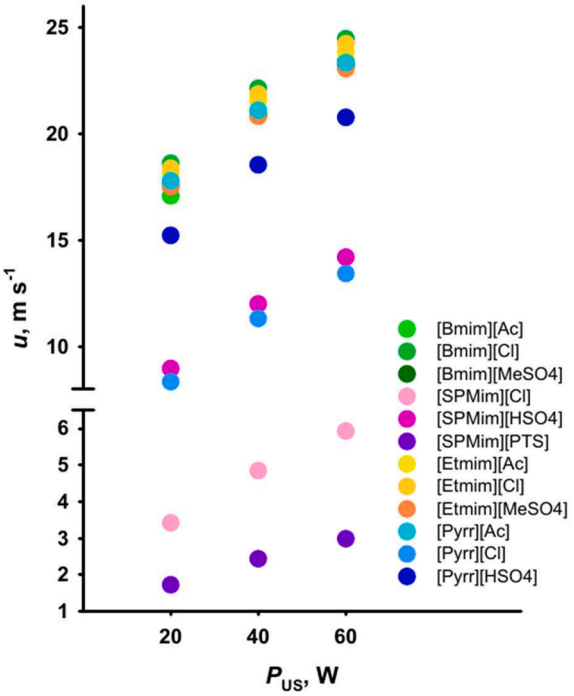

Fig. 13. u vs P_{US} at $d = 2$ cm.

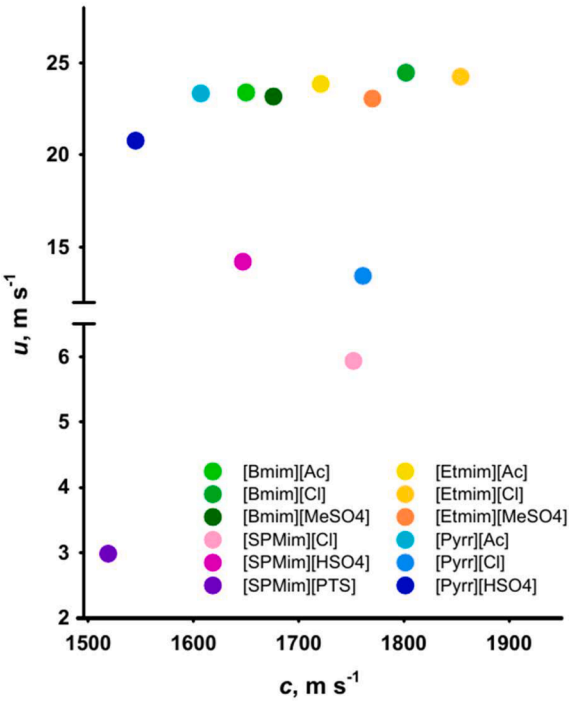

Fig. 14. u vs c at 60 W and $d = 2$ cm.

(Table 8).

8. Conclusions

Conducting experiments to study acoustic cavitation in liquid media other than water can be costly, particularly when a significant number of variables are involved in the experimental design. In such cases, numerical modelling has emerged as a particularly useful approach, as it enables the investigation of a vast array of parameters at a fraction of the

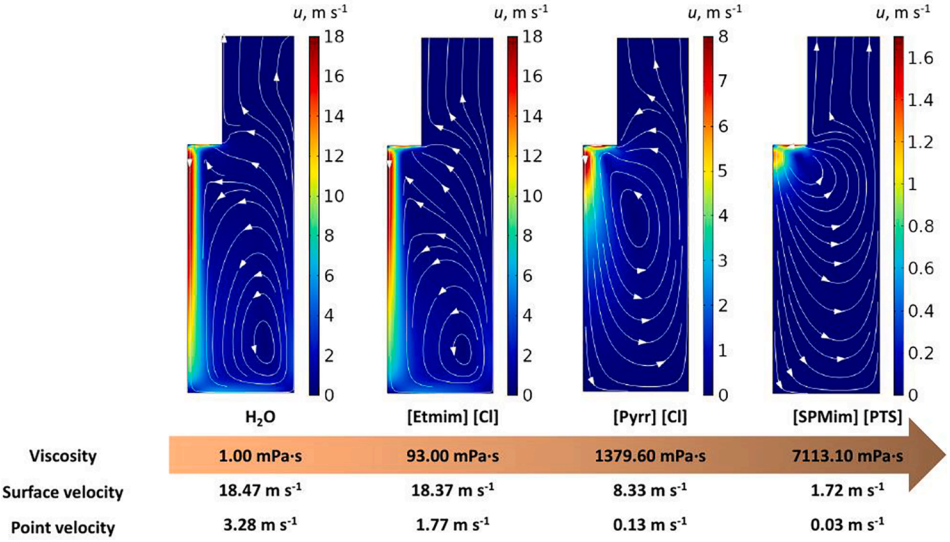

Fig. 15. u of water, [Etmim][Cl], [Pyrr][Cl], and [SPMim][PTS] at 20 W and d = 2 cm. u decreases with the increase of μ.

Table 8
Predictor screening analysis of u. Statistic significance in descending order. *Portion of the variance explained by the predictor.

Predictor	Portion*
P_{US}	56.25 %
μ	26.4 %
c	8.2 %
C_P	6.0 %
ρ	2.7 %
σ	<0.1 %
d	<0.1 %

cost. In this study, we characterized the acoustic cavitation in twelve ILs in a horn-type ultrasound reactor. We developed a model that takes into account the presence of numerous cavitation bubbles in the sonicated medium. The model incorporates the acoustic impedance mismatch at the geometrical boundaries of the simulation domain, and treats the ILs as incompressible, Newtonian, and saturated with argon. The experimental design studied the effect of ultrasound input power, probe immersion depth, and five ILs' thermodynamic properties on the acoustic pressure field, the volume of the active regions, and on the velocity of the acoustic streaming jet. The present study is the first to consider a large number of ionic liquids with such a diverse range of thermodynamic properties. A predictor screening analysis determined the portion of the variance explained by each independent variable. The non-linear regression of the simulation data provided five equations correlating acoustic pressure, active region volume, and streaming velocity to the variables contributing the most to the variance of the dataset. Viscosity is the most significant thermodynamic property on all the response variables except the maximum acoustic pressure. The US input power is significant on all variables but the minimum acoustic pressure. Specifically, the volume of the active regions and the magnitude of the acoustic streaming field increase with the increase of ultrasound power and the decrease of viscosity, whereas the magnitude of the minimum acoustic pressure increases with ultrasound power and viscosity. Probe immersion depth positively correlates with the active region volume and negative acoustic pressure at low viscosity, but its impact on the maximum acoustic streaming surface velocity and maximum acoustic pressure is insignificant (p-value > 0.05). 1-ethyl-3-methylimidazolium- and 1-butyl-3-methylimidazolium-based ILs yielded the largest active region volumes and the fastest acoustic jets. At 60 W and d = 2 cm, [Etmim][Cl] generates $V = 0.77$ cm^3 and $u = 24.2$ m s^{-1}, while [Bmim][Cl] produces $V = 0.76$ cm^3 and $u = 24.4$ m s^{-1}. 1-methyl-3-(3-sulfopropyl)-imidazolium-based ILs generated the smallest active region volumes and lowest maximum acoustic streaming surface velocities – 0.17 cm^3 and 1.72 m s^{-1} for [SPMim][PTS] at 20 W. Sonochemiluminescence experiments validated the results obtained through numerical simulation. This study advances the understanding of acoustic cavitation behaviour in ionic liquids and provides valuable insights for optimizing ultrasound-assisted processes in these solvents, whose application have become more and more frequent due to their tunable properties. Future research will address some limitations of this study, such as the fact that the hygroscopicity of some of the ILs was neglected and the thermodynamic properties of the ionic liquid were considered independent of temperature, which is equivalent to simulating the first stages of a sonication process. Because the ultrasound probe vibrates, there is a vertical displacement occurring at the liquid-probe boundary. Future investigations should consider the ultrasound tip as a moving wall rather than a fixed wall. Additionally, this study focused on argon gas to saturate the liquid, leaving room for investigation of other gases.

CRediT authorship contribution statement

Dalma Schieppati: Conceptualization, Data curation, Formal analysis, Investigation, Writing – original draft. **Mood Mohan:** Data curation, Software. **Bruno Blais:** Investigation, Validation, Writing – review & editing. **Kobra Fattahi:** Investigation, Software. **Gregory S. Patience:** Supervision, Software, Data curation, Writing – review & editing. **Blake A. Simmons:** Supervision, Validation, Writing – review & editing. **Seema Singh:** Software, Validation, Writing – review & editing. **Daria C. Boffito:** Supervision, Resources, Conceptualization, Validation, Writing – review & editing.

Declaration of competing interest

The authors declare that they have no known competing financial interests or personal relationships that could have appeared to influence the work reported in this paper.

Data availability

Data will be made available on request.

Acknowledgements

This research was undertaken, in part, thanks to funding from the Canada Research Chair program. Dalma Schieppati is thankful to the Natural Sciences and Engineering Research Council of Canada (NSERC) and to Fondation et Almuni de Polytechnique Montréal and Fayolle Canada for awarding her a Vanier Canada Graduate Scholarship and Bourse 'Prestige' États-Unis, respectively, to support her doctoral studies.

The portion of the work carried out by the Joint BioEnergy Institute (https://www.jbei.org) was supported by the DOE, Office of Science, Office of Biological and Environmental Research under contract DE-AC02-05CH11231 with Lawrence Berkeley National Laboratory.

The authors are thankful to Francesco G. Qualizza for providing the camera equipment and rendering valuable assistance during the sono-chemiluminescence experiments.

References

[1] D. Schieppati, A. Dreux, W. Gao, P. Fatehi, D.C. Boffito, Ultrasound-assisted carboxymethylation of LignoForce Kraft lignin to produce biodispersants, J. Clean. Prod. 366 (2022), 132776.
[2] P. Louyot, C. Neagoe, F. Galli, C. Pirola, G.S. Patience, D.C. Boffito, Ultrasound-assisted impregnation for high temperature Fischer-Tropsch catalysts, Ultrason. Sonochem. 48 (2018) 523–531.
[3] K.S. Suslick, G.J. Price, Applications of ultrasound to materials chemistry, Annu. Rev. Mater. Sci. 29 (1) (1999) 295–326.
[4] N. Patience, D. Schieppati, D. Boffito, Continuous and pulsed ultrasound pectin extraction from navel orange peels, Ultrason. Sonochem. 73 (2021), 105480.
[5] T. Leong, M. Ashokkumar, S. Kentish, The fundamentals of power ultrasound: a review, Acoustics Australia 39 (2) (2011) 54–63.
[6] E.B. Flint, K.S. Suslick, The temperature of cavitation, Science 253 (5026) (1991) 1397–1399.
[7] K.S. Suslick, S. Doktycz, E. Flint, On the origin of sonoluminescence and sonochemistry, Ultrasonics 28 (5) (1990) 280–290.
[8] D. Meroni, R. Djellabi, M. Ashokkumar, C.L. Bianchi, D.C. Boffito, Sonoprocessing: from concepts to large-scale reactors, Chem. Rev. 122 (3) (2021) 3219–3258.
[9] D. Boffito, F. Galli, C. Pirola, C. Bianchi, G. Patience, Ultrasonic free fatty acids esterification in tobacco and canola oil, Ultrason. Sonochem. 21 (6) (2014) 1969–1975.
[10] D.-J. Tao, Y. Dong, Z.-J. Cao, F.-F. Chen, X.-S. Chen, K. Huang, Tuning the acidity of sulfonic functionalized ionic liquids for highly efficient and selective synthesis of terpene esters, J. Ind. Eng. Chem. 41 (2016) 122–129.
[11] P.D. McCrary, P.A. Beasley, G. Gurau, A. Narita, P.S. Barber, O.A. Cojocaru, R. D. Rogers, Drug specific, tuning of an ionic liquid's hydrophilic–lipophilic balance to improve water solubility of poorly soluble active pharmaceutical ingredients, New J. Chem. 37 (7) (2013) 2196–2202.
[12] B.D. Rabideau, M. Soltani, R.A. Parker, B. Siu, E.A. Salter, A. Wierzbicki, K.N. West, J.H. Davis, Tuning the melting point of selected ionic liquids through adjustment of the cation's dipole moment, PCCP 22 (21) (2020) 12301–12311.
[13] F. Philippi, D. Rauber, O. Palumbo, K. Goloviznina, J. McDaniel, D. Pugh, S. Suarez, C.C. Fraenza, A. Padua, C.W. Kay, et al., Flexibility is the key to tuning the transport properties of fluorinated imide-based ionic liquids, Chem. Sci. 13 (32) (2022) 9176–9190.
[14] G.V. Carrera, C.A. Afonso, L.C. Branco, Interfacial properties, densities, and contact angles of task specific ionic liquids, J. Chem. Eng. Data 55 (2) (2010) 609–615.
[15] D.J. Flannigan, S.D. Hopkins, K.S. Suslick, Sonochemistry and sonoluminescence in ionic liquids, molten salts, and concentrated electrolyte solutions, J. Organomet. Chem. 690 (15) (2005) 3513–3517.
[16] K. Yasui, K. Yasui, Acoustic cavitation, Springer, 2018.
[17] K. Fattahi, E. Robert, D.C. Boffito, Numerical and experimental investigation of the cavitation field in horn-type sonochemical reactors, Chemical Engineering and Processing-Process Intensification 182 (2022), 109186.
[18] M. Mohan, K. Huang, V.R. Pidatala, B.A. Simmons, S. Singh, K.L. Sale, J. M. Gladden, Prediction of solubility parameters of lignin and ionic liquids using multi-resolution simulation approaches, Green Chem. (2022).
[19] Clarivate Analytics, Web of science core collection, accessed in February 2023, http://apps.webofknowledge.com (2022).
[20] A.N. Masri, M.A. Mutalib, N.F. Aminuddin, J.-M. Lévêque, Novel so3h-functionalized dicationic ionic liquids–a comparative study for esterification reaction by ultrasound cavitation and mechanical stirring for biodiesel production, Sep. Purif. Technol. 196 (2018) 106–114.
[21] P.M. Kanthale, M. Ashokkumar, F. Grieser, Estimation of cavitation bubble temperatures in an ionic liquid, J. Phys. Chem. C 111 (50) (2007) 18461–18463.
[22] P.M. Kanthale, A. Brotchie, F. Grieser, M. Ashokkumar, Sonoluminescence quenching and cavitation bubble temperature measurements in an ionic liquid, Ultrason. Sonochem. 20 (1) (2013) 47–51.
[23] J.D. Oxley, T. Prozorov, K.S. Suslick, Sonochemistry and sonoluminescence of room-temperature ionic liquids, J. Am. Chem. Soc. 125 (37) (2003) 11138–11139.
[24] B. Naidji, L. Hallez, A.E. Taouil, M. Rebetez, J. Hihn, Influence of pressure on ultrasonic cavitation activity in room temperature ionic liquids: An electrochemical study, Ultrason. Sonochem. 54 (2019) 129–134.
[25] B. Naidji, L. Hallez, A.E. Taouil, M. Rebetez, J. Hihn, Effect of cavitation intensity control on self-assembling of alkanethiols on gold in room temperature ionic liquids, Ultrason. Sonochem. 75 (2021), 105610.
[26] M.-H. Duan, M. Luo, C.-J. Zhao, W. Wang, Y.-G. Zu, D.-Y. Zhang, X.-H. Yao, Y.-J. Fu, Ionic liquid-based negative pressure cavitation assisted extraction of three main flavonoids from the pigeonpea roots and its pilot-scale application, Sep. Purif. Technol. 107 (2013) 26–36.
[27] M. Keswani, S. Raghavan, P. Deymier, Effect of non-ionic surfactants on transient cavitation in a megasonic field, Ultrason. Sonochem. 20 (1) (2013) 603–609.
[28] H.-X. Zhang, B. Gao, Y.-T. Yang, S.-Y. Zhang, X.-J. Liu, Numerical simulations of the cavitation process in a room-temperature ionic liquid, in symposium on piezoelectricity acoustic waves, and device applications, IEEE 2013 (2013) 1–3.
[29] H.G. Flynn, Cavitation dynamics. i. a mathematical formulation, J. Acoust. Soc. Am. 57 (6) (1975) 1379–1396.
[30] S. Merouani, O. Hamdaoui, B. Haddad, Acoustic cavitation in 1-butyl-3-methylimidazolium bis (triflluoromethyl-sulfonyl) imide based ionic liquid, Ultrason. Sonochem. 41 (2018) 143–155.
[31] K. Kerboua, O. Hamdaoui, A. Alghyamah, Acoustic cavitation events and solvation power of ionic liquid in a novel hybrid technique: A concept proposal toward a green pathway for cellulose decomposition, Ultrason. Sonochem. 73 (2021), 105469.
[32] S. Glegg, W. Devenport, Linear acoustics, in: B. Guerin (Ed.), Aeroacoustics of Low Mach Number Flows: Fundamentals, Analysis, and Measurement, Academic Press, 2017, pp. 49–72, https://doi.org/10.1016/B978-0-12-809651-2.00003-5.
[33] S.S. Rashwan, I. Dincer, A. Mohany, Investigation of acoustic and geometric effects on the sonoreactor performance, Ultrason. Sonochem. 68 (2020), 105174.
[34] R. Liu, Z. Li, The effects of bubble scattering on sound propagation in shallow water, Journal of Marine Science and Engineering 9 (12) (2021) 1441.
[35] L. Bjørnø, Scattering of sound, in: Applied Underwater Acoustics, Elsevier, 2017, pp. 297–362.
[36] T. Leighton, The acoustic bubble, Academic press, 2012.
[37] L. Van Wijngaarden, On the equations of motion for mixtures of liquid and gas bubbles, J. Fluid Mech. 33 (3) (1968) 465–474.
[38] L.V. Wijngaarden, One-dimensional flow of liquids containing small gas bubbles, Annu. Rev. Fluid Mech. 4 (1) (1972) 369–396.
[39] K.W. Commander, A. Prosperetti, Linear pressure waves in bubbly liquids: Comparison between theory and experiments, J. Acoust. Soc. Am. 85 (2) (1989) 732–746.
[40] R. Jamshidi, B. Pohl, U.A. Peuker, G. Brenner, Numerical investigation of sonochemical reactors considering the effect of inhomogeneous bubble clouds on ultrasonic wave propagation, Chem. Eng. J. 189 (2012) 364–375.
[41] Y. Fang, T. Yamamoto, S. Komarov, Cavitation and acoustic streaming generated by different sonotrode tips, Ultrason. Sonochem. 48 (2018) 79–87.
[42] J. Lighthill, Acoustic streaming, J. Sound Vib. 61 (3) (1978) 391–418.
[43] M.J. Lighthill, On sound generated aerodynamically i. general theory, Proc. R. Soc. Lond. A 211 (1107) (1952) 564–587.
[44] M.J. Lighthill, On sound generated aerodynamically ii. turbulence as a source of sound, Proc. R. Soc. Lond. A 222 (1148) (1954) 1–32.
[45] L. Zarembo, Acoustic streaming, in: High-intensity ultrasonic fields, Springer, 1971, pp. 135–199.
[46] J. Stuart, Unsteady boundary layers (unsteady boundary layer flow, considering stokes, rayleigh and heisenberg-tollmien theories application to oscillatory, fluctuating, impulsive and rotational effects), Recent Research on Unsteady Boundary Layers (1972) 1–59.
[47] Z. Gu, J.F. Brennecke, Volume expansivities and isothermal compressibilities of imidazolium and pyridinium-based ionic liquids, J. Chem. Eng. Data 47 (2) (2002) 339–345.
[48] M. Kambic, R. Kalb, T. Tasner, D. Lovrec, High bulk modulus of ionic liquid and effects on performance of hydraulic system, Scientific World Journal 2014 (2014).
[49] M.J. Kaiser, E. McAllister, Pipeline Rules of Thumb Handbook: A Manual of Quick, Gulf Professional Publishing, Accurate Solutions to Everyday Pipeline Engineering Problems, 2022.
[50] S. Dähnke, K. Swamy, F. Keil, Modeling of three-dimensional pressure fields in sonochemical reactors with an inhomogeneous density distribution of cavitation bubbles: comparison of theoretical and experimental results, Ultrason. Sonochem. 6 (1–2) (1999) 31–41.
[51] G. Servant, J.-L. Laborde, A. Hita, J.-P. Caltagirone, A. Gérard, Spatio-temporal dynamics of cavitation bubble clouds in a low frequency reactor: comparison between theoretical and experimental results, Ultrason. Sonochem. 8 (3) (2001) 163–174.
[52] M.C. Gomes, P. Husson, J. Jacquemin, V. Majer, Interactions of gases with ionic liquids: experimental approach, ACS Publications (2005).
[53] B. Gielen, S. Marchal, J. Jordens, L. Thomassen, L. Braeken, T. Van Gerven, Influence of dissolved gases on sonochemistry and sonoluminescence in a flow reactor, Ultrason. Sonochem. 31 (2016) 463–472.
[54] B. Avvaru, A.B. Pandit, Oscillating bubble concentration and its size distribution using acoustic emission spectra, Ultrason. Sonochem. 16 (1) (2009) 105–115.
[55] A. Li, R. Zhong, X. Li, J. Zhang, Enhancement of sonochemical efficiency using combination of ultrasound with ultraviolet irradiation and water flow in a horn-type reactor, Chemical Engineering and Processing-Process Intensification 150 (2020), 107884.

[56] F.J. Trujillo, K. Knoerzer, A computational modeling approach of the jet-like acoustic streaming and heat generation induced by low frequency high power ultrasonic horn reactors, Ultrason. Sonochem. 18 (6) (2011) 1263–1273.
[57] V. Girault, P.-A. Raviart, Finite Element Methods for Navier-Stokes Equations: Theory and Algorithms, Vol. 5, Springer Science & Business Media, 2012.
[58] J. Palomar, V.R. Ferro, J.S. Torrecilla, F. Rodríguez, Density and molar volume predictions using cosmo-rs for ionic liquids. an approach to solvent design, Ind. Eng. Chem. Res. 46 (18) (2007) 6041–6048.
[59] Z. Dai, Y. Chen, C. Liu, X. Lu, Y. Liu, X. Ji, Prediction and verification of heat capacities for pure ionic liquids, Chin. J. Chem. Eng. 31 (2021) 169–176.
[60] M. Mohan, B.A. Simmons, K.L. Sale, S. Singh, Multiscale molecular simulations for the solvation of lignin in ionic liquids, Sci. Rep. 13 (1) (2023) 271.
[61] F. Gharagheizi, P. Ilani-Kashkouli, A.H. Mohammadi, D. Ramjugernath, D. Richon, Development of a group contribution method for determination of viscosity of ionic liquids at atmospheric pressure, Chem. Eng. Sci. 80 (2012) 326–333.
[62] R.L. Gardas, J.A. Coutinho, Estimation of speed of sound of ionic liquids using surface tensions and densities: a volume-based approach, Fluid Phase Equilib. 267 (2) (2008) 188–192.
[63] M. Mohan, M.D. Smith, O.N. Demerdash, B.A. Simmons, S. Singh, M.K. Kidder, J. C. Smith, Quantum chemistry-driven machine learning approach for the prediction of the surface tension and speed of sound in ionic liquids, ACS Sustain. Chem. Eng. (2023).
[64] M. Mohan, M.D. Smith, O.N. Demerdash, B.A. Simmons, S. Singh, M.K. Kidder, J. C. Smith, Predictive understanding the surface tension and velocity of sound in ionic liquids using machine learning, ACS Sustain. Chem. Eng. (2023).
[65] M. Sattari, F. Gharagheizi, P. Ilani-Kashkouli, A.H. Mohammadi, D. Ramjugernath, Development of a group contribution method for the estimation of heat capacities of ionic liquids, J. Therm. Anal. Calorim. 115 (2014) 1863–1882.
[66] J.A. Lazzús, G. Pulgar-Villarroel, A group contribution method to estimate the viscosity of ionic liquids at different temperatures, J. Mol. Liq. 209 (2015) 161–168.
[67] J. Rumble, CRC Handbook of Chemistry and Physics (2017).
[68] M. Ashokkumar, F. Cavalieri, F. Chemat, K. Okitsu, A. Sambandam, K. Yasui, B. Zisu, Handbook of ultrasonics and sonochemistry, Springer Singapore, 2016.
[69] G. Kozmus, J. Zevnik, M. Hočevar, M. Dular, M. Petkovšek, Characterization of cavitation under ultrasonic horn tip–proposition of an acoustic cavitation parameter, Ultrason. Sonochem. 89 (2022), 106159.
[70] V. Salinas, Y. Vargas, O. Louisnard, L. Gaete, Influence of the liquid viscosity on the formation of bubble structures in a 20 khz field, Ultrason. Sonochem. 22 (2015) 227–234.